Numerical and experimental investigations of wave propagation in Kelvin Cell-based periodic lattice architectures

L. Kleine-Wächter [1,2], **R. Rumpler** [2,3], **H. Mao** [2,3], **P. Göransson** [2,3], **G. Müller** [1]
[1] TU Munich, Department of Civil and Environmental Engineering,
Arcisstr. 21, D-80333, Munich, Germany

[2] KTH Stockholm, Department of Engineering Mechanics,
Teknikringen 8, SE-10044 Stockholm, Sweden
e-mail: **lukas.kleinewaechter@tum.de**

[3] The Centre for ECO2 Vehicle Design,
Teknikringen 8, SE-10044 Stockholm, Sweden

Abstract
This contribution addresses elastic waveguiding properties of 1D-periodic lattice microstructures derived from the Kelvin cell. The Kelvin cell serves as a lattice template to subsequently introduce microstructural changes by imposing twists on the cell's square faces. Such modifications break the cell mirror symmetries and offer the possibility to adjust the wave filtering characteristics based on the twist angle and choice of tesselation. Band structure analyses reveal that altering the template geometry enforces frequency gaps stemming from coupled longitudinal-torsional modes and Bragg scattering. To validate the applicability of Kelvin cell lattice structures for vibration control, finite-size samples are manufactured from SLA-printing and tested in terms of transmission spectra. The experimentally observed frequency regions of reduced transmission correspond well with the band gap layout. Simulations of finite-size samples show that visco-elastic and frequency-dependent material behavior must be accounted for to numerically predict the measured transmission characteristics.

1 Introduction

The characteristics of materials are determined by their basic atomic building units and their structural arrangement [1]. To a degree, *mechanical* material properties can be regarded as the result of the microstructural composition and are observable on scales that differ by orders of magnitude from those of the microstructure. In developing novel materials, this principle is often mimicked by engineering microstructures from available materials in an attempt to control the emerging properties of the resulting structure up to the desired extent. These artificially generated properties can qualitatively or quantitatively exceed the properties of the constitutive material, which inspired the term *"metamaterial"* [2].

Among the different directions of material development, *lattice-type materials* are a much-noticed design paradigm [3]. Their microstructure typically comprises cellular units of interlaced trusses periodically repeated in space. The formation of truss-based networks offers vast design capabilities to attain unusual properties on the macroscopic level. In mechanics, vanishing shear stiffness at a finite bulk modulus [4], negative POISSON ratio [5], and frequency band gaps [6] are but a few examples of unique properties obtained from architected lattices.

The ability to generate tunable band gaps makes lattice-type materials particularly attractive for vibroacoustic applications. Band gaps are regions in the wavenumber-frequency spectrum where the free wave propagation is inhibited. In practice, this property manifests itself in a substantial attenuation of wave propagation in the band gap frequency ranges [7]. From a physical point of view, the wave filtering functionality originates from different mechanisms whose occurrence strongly depends on the lattice configuration. If the wavelength of

Figure 1: Isometric Kelvin cell reference and coordinate definitions (left) and geometry after twisting all six square faces (right) [16].

propagating waves matches the lattice periodicity, waves scattered within the lattice interfere destructively, leading to BRAGG-scattering. Due to the mechanism's dependency on the lattice dimensions, achieving band gaps in the low-frequency region is complicated as large periodicity constants are required. Embedding substructural units for resonant behaviour provides a remedy to attain band gaps independent of the lattice periodicity. The substructural unit's resonant coupling to the motion of the host structure is dictated by ratios of mass and stiffness [6]. Several studies have shown that adding point-like masses to a host lattice facilitates significant band gaps [8, 9]. However, the required mass addition may be severe, mainly when targeting low frequencies.

Therefore, other concepts seek to induce band gaps by manupulating the topological features of lattice microstructures. Hierarchical architectures consist of cellular units tessellated on multiple scales, evoking band gaps in various frequency regimes [10]. On the level of the unit cell itself, *chirality*, i. e., the lack of mirror symmetries is a promising design paradigm. Cellular lattice units with chiral symmetry can, among other effects, enforce coupling of rotational and translational deformations, such that an additional inertia factor enters the dynamics of the chiral lattice [11]. By amplifying this inertia term using well-defined mass elements, significant band gaps in the low-frequency regime are attainable with a minimal mass penalty [12]. By introducing *tacticity*, i. e. alternating the handedness of chiral units in the lattice, significant band gaps are achievable without additional mass requirement or changing the stiffness features [13].

However, effects stemming from chirality are often only available in a specific direction, which may limit the application possibilities of these lattices. Furthermore, the complexity of hierarchical and chiral lattice microstructures is a significant obstacle to manufacturing and impedes application. Especially at small scales, advanced manufacturing techniques such as 3D laser nanoprinting are required [14], which renders the production of the material microstructure more costly and impractical compared to more straightforward, non-chiral architectures.

This paper attempts to contribute to the research of lattice-type microstructures for vibration control by investigating lattice architectures derived from the KELVIN cell shown in Fig. 1. By imposing so-called *twists* on the KELVIN cell, the geometrical features of the resulting microstructure can be fundamentally altered on the level of the unit cell and its tessellations [15]. While the KELVIN cell is not a priori optimised for vibration control in contrast to mentioned examples from the literature, it is chosen as template design since it tackles two areas on which the authors believe that more in-depth attention should be paid: First, its comparatively simple basic structure and the straightforward parametrisation of geometrical alterations offer a variety of possibilities for changing the lattice architecture, e.g. from achiral to chiral, in a controlled manner. The resulting properties –such as band gap behaviour for vibration attenuation– are thus observable as a function of the change at the microstructural level. Second, the derived lattice architectures are manufacturable with conventional 3D printing techniques at comparatively low costs and, therefore, accessible for experimental investigations, as discussed in Sec. 4 of this paper.

2 Kelvin cell-based lattice architectures

An adjustable unit cell approach, as initially proposed by some of the co-authors, is adopted to facilitate controllable modifications of the microstructural outline, which considers the isometric KELVIN cell as a geometrical template [15]. The basic geometric structure shown in Fig. 1 consists of two opposing square surfaces along the three principal directions. Connecting adjacent square faces creates a network of 36 ligaments, which is the basic cellular unit as presented in Fig. 2a. In this configuration, the cell exhibits isometry with a characteristic length h_c along the three principal directions.

Geometrical modifications imposed to the template geometry are achieved through coordinate transformations that describe pairwise in-plane rigid body rotations of the square faces, as illustrated in Fig. 1. The direction of rotation applied to opposite square faces leads to either symmetric or anti-symmetric configurations, meaning clockwise or counter-clockwise rotations of opposing faces. While the twisting approach changes the location of ligament vertices, it does not affect the ligament connection pattern such that all vertices remain connected through the same ligaments. Therefore, modified structures are topologically equivalent to the isometric KELVIN cell, and all twisted faces remain in their original planes, meaning that generated lattice architectures retain a simple-cubic nature.

Mathematically, the *twisting*-approach is expressed by transformations between the cell's local and global coordinate systems using Euler rotation angles $[\theta_j^{\hat{x}}, \theta_j^{\hat{y}}, \theta_j^{\hat{z}}]$. The sets of local coordinates $(\hat{x}, \hat{y}, \hat{z})_j$ originate in the center of the respective square faces denoted j and are parallel to the isometric cell's global coordinates (x, y, z) as shown in Fig. 1. Assuming successive, independent rotations around the axes $\hat{z}, \hat{y}$ and $\hat{x}$, the rotation matrices read

$$[R]_j = \begin{bmatrix} 1 & 0 & 0 \\ 0 & \mathrm{c}.\theta_j^{\hat{x}} & \pm\mathrm{s}.\theta_j^{\hat{x}} \\ 0 & \mathrm{s}.\theta_j^{\hat{x}} & \mathrm{c}.\theta_j^{\hat{x}} \end{bmatrix} \begin{bmatrix} \mathrm{c}.\theta_j^{\hat{y}} & 0 & \mathrm{s}.\theta_j^{\hat{y}} \\ 0 & 1 & 0 \\ \pm\mathrm{s}.\theta_j^{\hat{y}} & 0 & \mathrm{c}.\theta_j^{\hat{y}} \end{bmatrix} \begin{bmatrix} \mathrm{c}.\theta_j^{\hat{z}} & \pm\mathrm{s}.\theta_j^{\hat{z}} & 0 \\ \mathrm{s}.\theta_j^{\hat{z}} & \mathrm{c}.\theta_j^{\hat{z}} & 0 \\ 0 & 1 & 0 \end{bmatrix} \tag{1}$$

with $\mathrm{c}.\cdot = \cos(\cdot)$ and $\mathrm{s}.\cdot = \sin(\cdot)$. Consequently, the location of points $(\hat{x}, \hat{y}, \hat{z})_j^T$ at the square face j of the KC reference lattice is given by

$$\left(\hat{x}', \hat{y}', \hat{z}'\right)_j^T = [R]_j \left(\hat{x}, \hat{y}, \hat{z}\right)_j^T \tag{2}$$

after twisting the isometric structure. The twist angle and the respective rotation directions represent levers to alter the unit cell, which comes in addition to the choice of characteristic length and the diameter of the ligaments. While the twist angle affects the inclination of ligaments connecting the square faces, the direction of rotation impacts the unit cell's mirror symmetries. In particular, twisting all square faces in opposing directions creates chiral lattice configurations, as exemplified in Fig. 2c. Adjusting the alteration of square faces independently (Fig. 2b) provides the opportunity to create lattices with significant anisotropy in the emerging elastic properties [16].

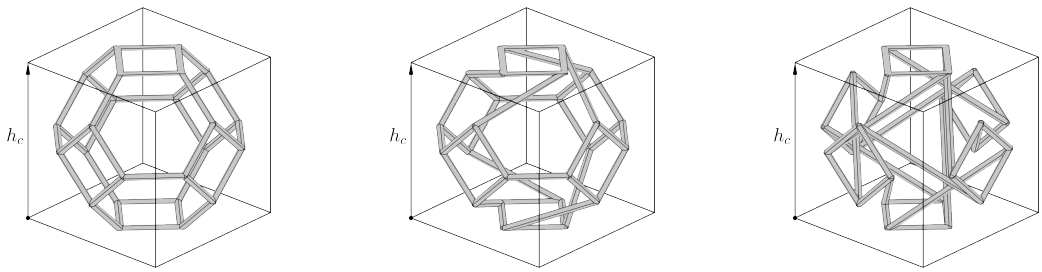

(a) Isometric Kelvin cell (b) One-axial twist (c) Three-axial twist (chiral cell)

Figure 2: Elementary cells obtained from the *twisting*-approach. Subfigure (a) is the template unit cell; examples (b) and (c) show a one- and three-axial twist modifications, respectively. Opposing the twist direction of square faces as in example (c) establishes chirality.

3 Wave dispersion analyses – Infinite periodicity

The effects of geometrical changes stemming from the outlined *twisting*-approach on the wave propagation features are first investigated by modelling the lattice microstructure as an infinitely extended medium. To simplify matters, the structures are only tessellated periodically along one direction so that spatial-periodic waveguides with Kelvin-cell-based microstructures are considered. Therefore, the lattice configurations are described by infinitely repeated unit cells, and the dispersion relation captures their *free* wave propagation characteristics.

3.1 Dispersion relation – Band structure calculation

Assuming linear-elastic, isotropic and homogeneous constituent material behavior, the wave propagation through the spatially periodic lattice structure is governed by the elastodynamic NAVIER-CAUCHY equation,

$$\frac{E}{2(1+\nu)(1-2\nu)}\nabla(\nabla\cdot\boldsymbol{u})+\frac{E}{2(1+\nu)}\nabla^2\boldsymbol{u}=-\rho\omega^2\boldsymbol{u}, \tag{3}$$

in the displacements $\boldsymbol{u}=[u_x,u_y,u_z]^{\mathrm{T}}$. Eq. (3) presumes time-harmonic dependency with angular frequency ω. E is the YOUNG'S modulus, ρ is the mass density, and ν is POISSON'S ratio of the constituent material. These parameters were set based on the polymer base material for later manufacturing (see Tab. 1). By virtue of the BLOCH-FLOQUET theory, the spatial periodicity of the medium is exploited to reduce the computational domain to a single representative unit cell Ω_{U}. The spatial solutions of the wave equation (3) take the form

$$\boldsymbol{u}\left(\boldsymbol{r},\boldsymbol{k}\right)=\tilde{\boldsymbol{u}}_{\boldsymbol{k}}\left(\boldsymbol{r},\boldsymbol{k}\right)\mathrm{e}^{-i\boldsymbol{k}\cdot\boldsymbol{r}}\text{ in }\Omega_{\mathrm{U}}, \tag{4}$$

with $\boldsymbol{k}$ the wave vector, $\boldsymbol{r}$ the position vector in the lattice, and $\tilde{\boldsymbol{u}}_{\boldsymbol{k}}$ the BLOCH-functions that share the periodicity of the lattice, i.e., $\tilde{\boldsymbol{u}}_{\boldsymbol{k}}(\boldsymbol{r})=\tilde{\boldsymbol{u}_{\boldsymbol{k}}}(\boldsymbol{r}+\boldsymbol{R})$ with $\boldsymbol{R}$ the reciprocal lattice vector. This contribution only considers one-dimensional periodic structures, which reduces the wave vector to $\boldsymbol{k}=[0,0,k_z]^T$ and demands periodicity at the domain boundary along one direction only, i.e.

$$\boldsymbol{u}(\boldsymbol{r})=\boldsymbol{u}(\boldsymbol{r}+\boldsymbol{a})\ \text{ on }\Gamma\Omega_{\mathrm{U}}, \tag{5}$$

with $\boldsymbol{a}=[0,0,a]$ the characteristic length of the lattice. All remaining boundaries of the unit cell are treated as traction free. Considering Eq. (4) and Eq. (5) in wave equation (3), standard argments in the Finite Element framework lead to the dispersion eigenvalue problem

$$\left[\mathbf{K}(k)-\omega^2\mathbf{M}\right]\tilde{\boldsymbol{u}}_{\boldsymbol{k}}=0, \tag{6}$$

with $\mathbf{K}$ and $\mathbf{M}$ being the stiffness and mass matrix in Finite Element notation, respectively [17]. The quadratic eigenvalue problem Eq. (6) is solved by imposing the angular frequencies $\{\omega_i,\mid i=1,\ldots,N_\omega\}$ and solving for the wave vector components k and corresponding BLOCH eigenvectors $\tilde{\boldsymbol{u}}_{\boldsymbol{k}_i}$. To this end, the finite element routines of the commercial software COMSOL MULTIPHYSICS are employed and all unit cell domains are discretized with tetrahedal elements. The resulting solution set $\{k(\omega_i),\mid i=1,\ldots,N_\omega\}$ is the *dispersion relation* of the free wave motion and presented in terms of the band structure by limiting the real part of the wave vector to the irreducible part of the BRILLOUIN zone such that $\mathrm{Re}\{k\}\in[0,\pi/a]$. The eigenvector components are averaged over the entire unit cell volume to a polarization factor

$$p_z(\omega,k)=\frac{\int_V|\boldsymbol{u}_z|^2\mathrm{d}V}{\int_V|\boldsymbol{u}_x|^2+|\boldsymbol{u}_y|^2+|\boldsymbol{u}_z|^2\mathrm{d}V}\ \in\ [0,1], \tag{7}$$

to color-code the band structure and distinguish the individual dispersion branches. Here, the z-direction is the axis along the waveguide. For ease of comparison, the eigenfrequencies are normalized with respect to the shear velocity $c_{\mathrm{s}}=\sqrt{G/\rho}$ of the bulk material and the characteristic length a such that $f^*=fa/c_{\mathrm{s}}$.

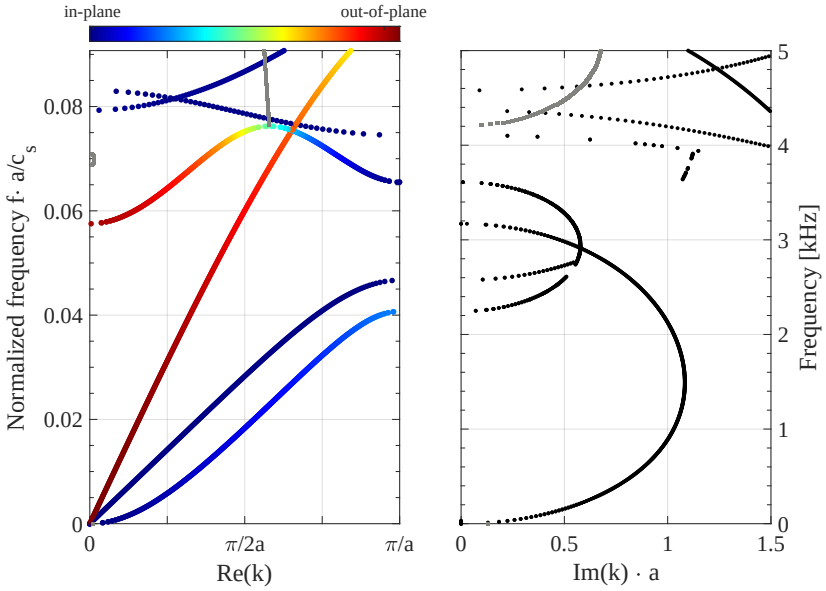

Figure 3: Dispersion relation of the isometric KELVIN cell for 1D-periodicity for eigenfrequencies between 0 kHz and 5 kHz. The colour-coding in the left panel highlights the dominating mode polarisation computed from Eq. (7) of propagating modes ($\mathrm{Im}(k) = 0$). Attenuated modes ($\mathrm{Im}(k)\,\&\,\mathrm{Re}(k) \neq 0$) are depicted by grey squares, while in the left panel, black dots represent evanescent modes ($\mathrm{Re}(k) = 0$). The real part of the wavenumber is restricted to the irreducible BRILLOUIN zone; the imaginary part is expressed in terms of the characteristic unit cell length a.

3.2 Dispersion relation of the isometric KELVIN cell

Fig. 3 reports the dispersion relation of the isometric KELVIN cell as shown in Fig. 2a under 1D-periodic translation for eigenfrequencies up to 5 kHz. Three fundamental branches originating from the zero point dominate the band structure in the considered frequency region. Towards the long wavelength limit $k \to 0$, the lattice structure supports wave motions corresponding to the solutions of a continuous, homogeneous, and linear-elastic waveguide: Among the transversely polarized modes (blue-coloured), the first branch exhibits *flexural* wave motions with main deflections in the xy-plane transverse to the direction of propagation. Modes of the second branch are governed by rotational deformations and along the propagation axis, corresponding to *torsional* waves. Finally, compression-extension wave motions are found in the third branch, highlighted in red and referred to as *longitudinal* polarization. Higher-order branches disperse non-linearly; here, shear motions of the individual lattice struts govern corresponding mode shapes. The band structure does not reveal any full band gap in the frequency region of interest. However, the infinitely repeated unit cell only supports longitudinally polarised modes in the normalized frequency regime in the vicinity of $f^* = 0.05$.

3.3 Exemplary twisted arrangement & band gap mechanisms

The potential of manipulating the eigenvalue spacing of the KELVIN cell unit by introducing microstructural changes in terms of the twisting approach is exemplified by utilising the unit cell presented in Fig. 4. For this case study, the changes are kept to a minimum by twisting the top face only with an angle of $\theta_z^+ = 45°$. The induced disorientation of the square face breaks the cell's mirror symmetry, rendering the opposing bottom and twisted top faces non-imposable. Therefore, a periodic tessellation through pure translations is not permitted. Instead, a glide-symmetry is introduced by reflecting the twisted cellular unit with respect to the transverse plane at the unit cell boundary. This operation merges the twisted and untwisted square faces along the waveguide axis, and creates a supercell unit with doubled translation periodicity $\hat{a} = 2\mathrm{a}$. The introduced modification thus consists of the geometry modification on the unit cell level and the imposed tessellation.

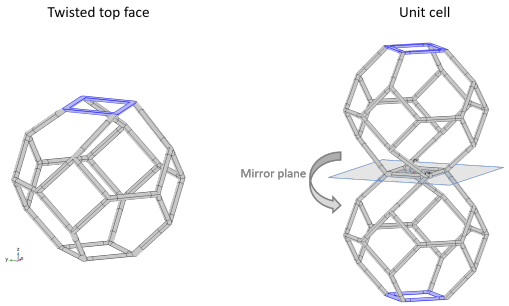

Figure 4: The left-hand figure displays a cellular building block with only its top face (highlighted in blue) twisted by $\theta^{\hat{z}}_{z_+} = 45°$ with respect to the isometric KELVIN cell. As this operation creates non-matching cell boundaries, the cell is duplicated by a mirror-translation with respect to the illustrated horizontal plane. A unit cell with doubled characteristic length results, as shown on the right.

Fig. 5 displays the resulting band structure that is single-folded in the first BRILLOUIN zone, owing to the supercell approach. Two observations will be given priority as follows: First, the real part of the band structure reveals the occurrence of a band gap that emerges between the folded longitudinal branches at a normalized frequency around $f^* \approx 0.05$. In this frequency regime, only evanescent modes with a non-vanishing imaginary part exist, confirming the *full* stop band characteristic of the structure. Considering the dispersion properties of the KELVIN cell as discussed in Fig. 3, the changes introduced thus enable band gap formation. The imaginary part of the wavenumber inside the band gap region further suggests that wave scattering drives the band gap formation: The evanescent branch that connects the longitudinal modes at the edge of the BRILLOUIN zone varies continuously in a parabolic manner and reaches its maximum $\max\{\mathrm{Im}(k)\}$ in the vicinity of the middle frequency $f^* \approx 0.05$ between the split longitudinal branches. Such characteristic is typical for BRAGG-scattering, which refers to destructive interference of incoming and scattered waves and occurs as the wavelength becomes comparable to the unit cell size [18]. For longitudinal waves, BRAGG-type scattering occurs around the frequency $f_{\mathrm{Bragg}} \approx c_{\mathrm{p}}/2\mathrm{a}$, with c_{p} being the effective phase velocity of the longitudinal wave and a the characteristic length [19]. In the given case, the effective phase velocity is deduced from the long wavelength modes of the longitudinal branch near $k \to 0$, and yields the estimate $c_{\mathrm{p}} = \omega/k \approx 221\,\mathrm{m/s}$. The corresponding BRAGG-frequency thus results in $f_{\mathrm{Bragg}} \approx 2766\,\mathrm{Hz} \mathrel{\hat{=}} f^*_{\mathrm{Bragg}} = 0.05$, which perfectly matches the observed band gap region and provides further evidence for the gap mechanism.

The second observation concerns the frequency regime around $f^* = 0.035$ and involves wave propagation driven by coupling dynamics between propagating longitudinal and torsional modes. For a detailed analysis, Fig. 5b depicts the corresponding segment of the band structure with respect to the complex wavenumber plane. The dispersion relation shows a bifurcation pattern of the longitudinal and torsional branches in which both branches first attract and then repel each other for increasing wavenumbers. As a result, both branches have opposing slopes $\partial\omega/\partial k$, denoting the counter-propagation of their modes, and two turning points $\partial\omega/\partial k = 0$ that exhibit zero group velocity inside the BRILLOUIN zone. While the branches exchange their polarisation state after passing the turning point, the polarization values of zero group velocity modes merge at $p_z \approx 0.5$, which represents the averaged polarization of both branches. Here, longitudinal and torsional modes couple, causing a narrow-banded frequency gap for modes of both kinds. Inside this gap, there exist two branches of coupled modes with attenuated ($\mathrm{Im}(k) < 0$) and amplified ($\mathrm{Im}(k) > 0$) characteristics. For the existence of these and propagating flexural modes inside the frequency gap, it may not be classified as *full* band gap, but as a *"partial"* one that is enforced by mode coupling. It is worth mentioning that the coupling mechanism differs from local resonance phenomena, which involve the coupling of propagating modes with stationary ones of the resonant units for specific wavenumber-frequency combinations [20]. In contrast, the observed mechanism comprises the coupling of two counter-propagating waves whose group velocity is directed in opposing directions. The counter-propagation is a prerequisite for the occurrence of this coupling type and is facilitated by the symmetry configuration of the wave guide's micro-structure. In the given case, the mirror-reflection symmetry introduced between twisted cells creates a periodic configuration that reflects the torsional branch in the BRILLOUIN zone such that its propagation direction opposes the longitudinal one, leading to the observed interaction as both branches are about to cross. It should be noted

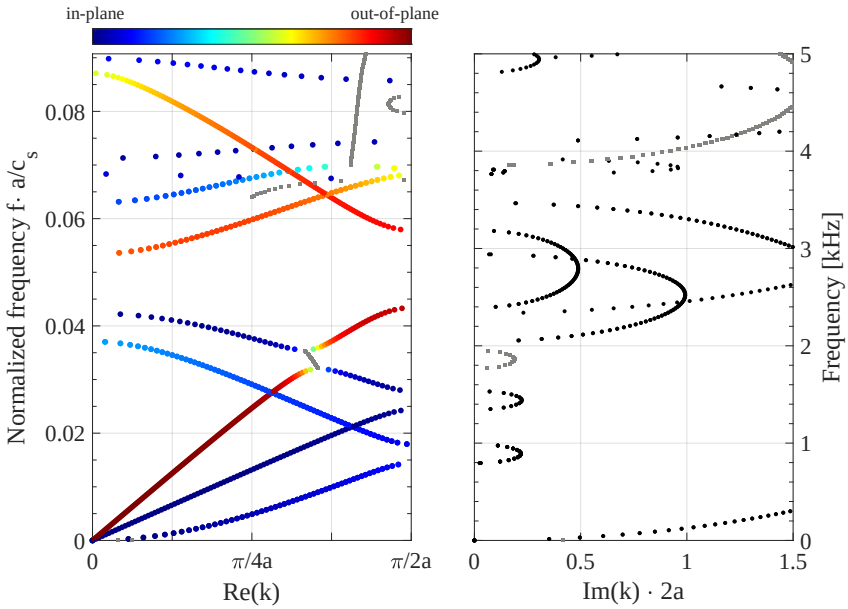

(a) Full band structure in the first irreducible BRILLOUIN zone and stop band region

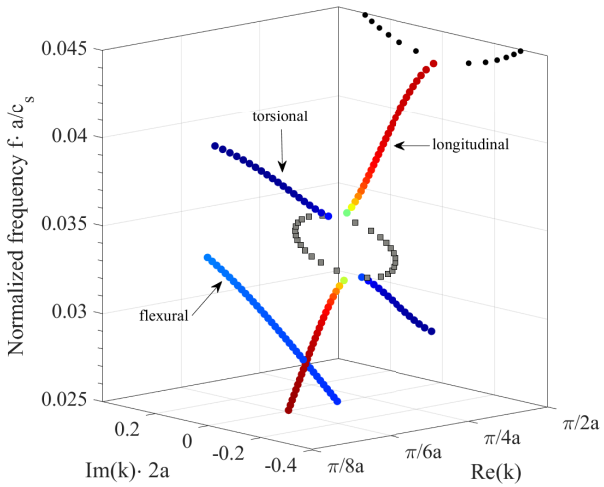

(b) Snippet of the full band structure shown in (a): Avoided crossing of the longitudinal and torsional branches displayed in the complex wavenumber plane.

Figure 5: Dispersion relation of the $45°$-twisted unit cell. The colour-coding highlights the dominating mode polarization computed from Eq. (7) of propagating modes ($\mathrm{Im}(k) = 0$). Attenuated modes ($\mathrm{Im}(k)$ & $\mathrm{Re}(k) \neq 0$) are depicted by grey squares, while black dots represent evanescent modes ($\mathrm{Re}(k) = 0$). The real part of the wavenumber is restricted to the irreducible BRILLOUIN zone; the imaginary part is expressed in terms of the characteristic unit cell length 2a.

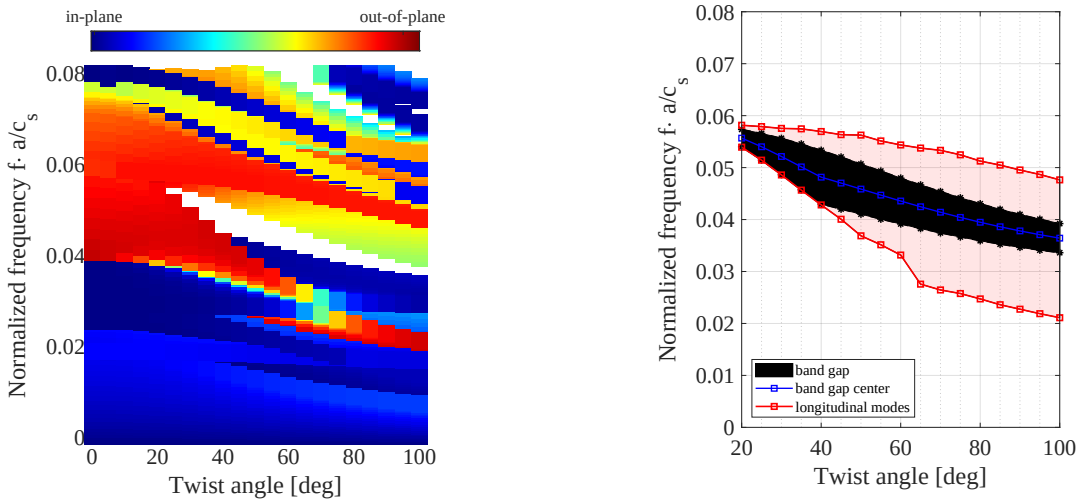

(a) Condensed dispersion relation. The color-coding highlights the dominant mode polarization from longitudinal (red) to in-plane/shear (blue). Blank regions denote full band gaps.

(b) Evolution of the BRAGG-type band gap and frequency split between the folded longitudinal branches at the BRILLOUIN zone edge as a function of the twist angle.

Figure 6: Effects of the twist angle on the eigenfrequency spacing and band gap tunability.

that this modification does not require adding local masses to the structure, as is the case for frequency gaps emerging from local resonances. In the literature, other terms referring to this coupling phenomenon are *mode lock-in, mode matching* [21, 22], and *avoided crossing* [23]. A detailed explanation of the dispersion features in coupled waveguides is presented by MACE *et al.* [24].

3.4 Effects of the twist angle on the band gap tunability

To investigate the dependency of the full BRAGG-type band gap on the twist angle, the dispersion analysis is repeated for gradually varying twist angles θ_z by $5°$ in the range of $[0°, 100°]$. To reduce the computational burden, only the *propagating* modes are solved for by using a standard $\omega(k)$ approach, often referred to as the *indirect* approach. The obtained eigenfrequency distribution $\omega(k, \theta_z)$ of the first irreducible BRILLOUIN zone is plotted in Fig. 6a with respect to the twist angle θ_z to condense the information of all band structures in a single diagram. Note that in contrast to the previous study, a smaller ligament diameter was selected in the parametric study. Due to the scale invariance of the wave equation (3), the dispersion relations do not change qualitatively, and statements about the impact of the twist angle on the band structure can still be made. The condensed dispersion diagram suggests that increasing the twist angle in the given unit cell configuration shifts propagating modes towards lower frequencies. While the mass addition due to twisting is minor compared to the connecting ligament extension and re-orientation, this tuning effect is stiffness-driven in connection with the effective axial stiffness of the unit cells. However, these stiffness-induced frequency shifts manifest themselves to varying degrees depending on the mode polarisation: While "in-plane" polarised modes (denoted in blue) are less affected, longitudinally polarised modes (colored red) are most receptive to changes of the twist angle. For these modes, the frequency split between the acoustic and optical branches increases with increasing twist angles; an observation that is analogous to the branch separation of a di-atomic mass-spring chain with diverging stiffness constants. As a result, the full band gap (highlighted in black) opens between angles of $20°$ and $100°$. Fig. 6b shows that increasing the twist angle lowers the band gap center frequency, but does not gradually widen the band gap as is the case for the longitudinal branch splitting. The widest band gap is identified at $40°$-twist angle with a relative width of $(f_{\mathrm{top}} - f_{\mathrm{bot}})/f_{\mathrm{mid}} = 21.5\,\%$ and slightly closes again for larger twist angles for "in-plane"-polarized modes being tuned down and bounding the band gap edges. In summary, the parametric study indicates that the twist angle provides a lever to modify both the band gap center and width, with the main constraints that the maximum band gap width is limited

and comes at the expense of a reduced axial stiffness of the unit cell. At the same time, the observed gradually increasing frequency split between the longitudinal branches offers the prospect of obtaining a wider wave attenuation range for forced vibration problems that excite the structure along its axis and thus predominantly trigger longitudinal vibrations. Such forced vibration problems at finite-size structure are subject of the subsequent experimental study.

4 Experimental validation – Transmission analysis

To examine the relevance of the observed band gap properties for the purpose of vibration attenuation, selected lattice structures with a finite number of unit cells were manufactured and experimentally tested. The frequency-dependent transmission of forced vibrations between two observation points in the lattice serves as a measure of the wave-filtering properties of the finite structures.

4.1 Manufacturing

Following the bang gap evolution in Fig. 6b, a unit cell configuration featuring a $45°$-twist angle was selected as a candidate for experimental validation and manufactured by 3D printing. The specimens consist of 1 x 1 x 3 arrays of twisted Kelvin cells units with a total length of $L = 12\,\mathrm{cm}$ and a characteristic length of $a = 4\,\mathrm{cm}$. Two thin square-shaped plates of width $w = 2\,\mathrm{cm}$ and a thickness of 1.5 mm were added at each end to enable later sensor mounting for the vibration transmission measurements. The lattice dimensions were set to accommodate arrays of at least three unit cells within the printer's available build volume. The ligament strut thickness is 1.5 mm, yielding a comparably low lattice relative density. The open-cell lattice architecture in connection with low relative densities renders the manufacturing process challenging. In the build phase, the lattice does not support itself but requires additional supports distributed along the entire geometry to prevent non-reversible deformation and collapse of the ligaments under gravity. To minimize the effects of build direction and layer height on the target properties, the layer thickness should be at scales smaller than the minimal geometrical details, e.g., the strut thickness. Consequently, laser-based 3D printing using a Stereolithographic apparatus (SLA) was chosen for its ability to manufacture specimens at a high level of detail. A commercial FORMLABS 3 SLA printer and FORMLABS resin type *Rigid 4k* as a base material were used; the thickness of each individual layer was 50 nm. After the build phase, the samples were cleaned from un-solidificated resin in an ultrasonic bath filled with isopropanol and post-cured for 20 minutes at $80\,°\mathrm{C}$ with $405\,\mathrm{nm}$ light in a FORMLABS cure oven. To avoid warping during the curing procedure, the temperature was gradually increased from room temperature to $80\,°\mathrm{C}$ with $1\,°\mathrm{C}$ per minute. The support structure was removed after the post-curing phase to prevent warpage of the specimens in each of the fabrication phases. The finished samples were then glued at one end with a 10-32 UNF-type screw printed from the same base material to minimize the impedance mismatch of the specimen and the connector of the vibration exciter.

4.2 Measurement setup

The specimens were screwed vertically in the vibration exciter (B&K Type 4810 and Type 2718 amplifying unit) as shown in Fig. 7. The in- and output velocity amplitudes were measured at the top and bottom plate in axial direction (parallel to the direction of wave propagation) with a POLYTEC OFV-5000 Laser Vibrometer. At each plate, two measurement points in central and eccentric position were in focus, and reflective tape was attached to the specimen to enhance the signal-to-noise ratio. The structures were excited with a linear

Table 1: Mechanical parameters of the constituent polymer used for the specimen fabrication. The elasticity modulus and density were taken from the data sheet of the used resin (type FORMLABS *Rigid 4k*).

YOUNG'S modulus E [GPa]	density ρ [kg/m^3]	POISSON'S ratio ν
4.1	1250	0.35

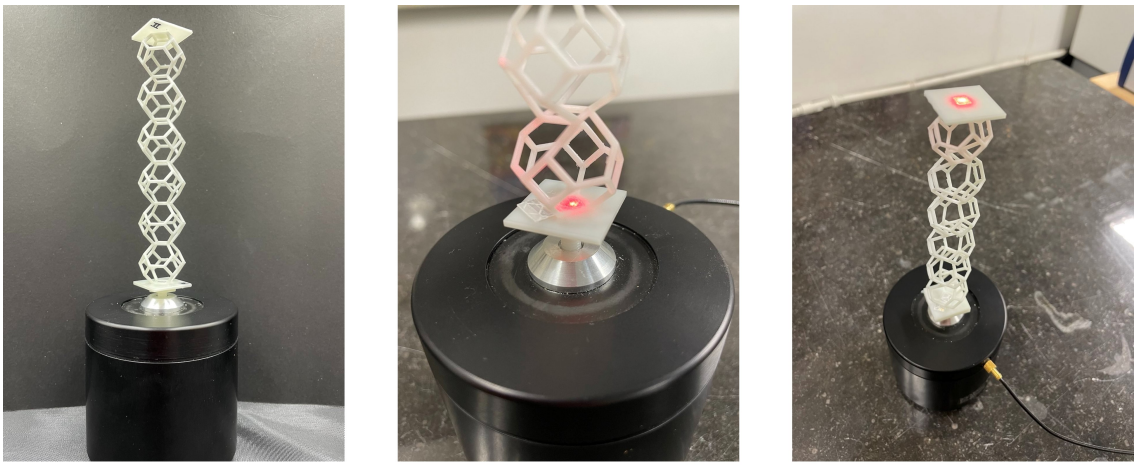

(a) (b) (c)

Figure 7: Setup for the transmission measurements. (a) Vertical alignment of a manufactured sample comprising three unit cells in the vibration exciter; (b) and (c): In- and output measurement points of the vibrometer at the bottom and top plate, respectively.

frequency sweep ranging from 100 Hz – 1 kHz in low-frequency and from 1 kHz–10 kHz in high-frequency for four seconds each. Signal generation, measurement triggering, and recording were realized with a SPECTRUM hybridNETBOX at 128 kHz sampling rate. For the high-frequency sweep, the output voltage of the input signal amplifier was carefully increased without reaching the distortion range of the amplifier to maximize the sensitivity and signal-to-noise ratio at the expected band gap frequency regions. The post-processing of the recorded time-domain data was done in MATLAB.

4.3 Experimental results

Fig. 8 shows the transmission spectrum obtained from the manufactured lattice structure. Along with the transmission, the figure presents the signal coherence computed from the recorded in- and output velocities in the frequency domain. The coherence values are close to one for a wide range of frequencies, indicating a good correlation of the input and output with low levels of noise and, therefore, a valid capture of the lattice structure's effects on signal transmission. The coherence function exhibited noise and dropped to values of 0.5 for frequencies beyond 8 kHz, so the subsequent analysis omits results for frequencies higher than the mentioned limit.

The coherence drop around 1 kHz identifies the combination point of two measurement data sets resulting from a low- and high-frequency sweep. The transmission spectrum displays three wide-ranging frequency regions of significant attenuation with center frequencies around 3 kHz, 6 kHz, and 7.3 kHz, respectively. Inside the latter regions, noise affects the transmitted signal, which underlines the strong attenuation in these regions and is also reflected in reduced coherence values at given frequencies. To validate the observed regions of attenuation with the predicted band gaps from the band structure analysis, Fig. 9 compares the band layout for infinite periodicity with the experimentally observed transmission spectrum for frequencies up to 5 kHz. The comparison shows good correspondence of both BRAGG- and coupling-type band gaps for infinite periodicity with the attenuation frequency regions at finite-size periodicity. In the coupling region, the transmission spectrum exhibits a resonance- and anti-resonance-like behaviour with a maximum attenuation of -11 dB, suggesting that the coupling mechanism provides less efficient wave attenuation at finite-size as compared to the BRAGG-type band gap. Here, the reduced transmission regimes correspond well with the splitting of the longitudinal branches as observable in the band layout and reach a maximum input-output reduction of $-20\,\mathrm{dB}$. The study confirms that the twisting-induced band gaps are real in manufactured structures, where only three finite-periodic unit cells already allow to achieve significant attenuation levels in this case. Finally, Fig. 10 compares the measured transmission spectra of the discussed twisted arrangement

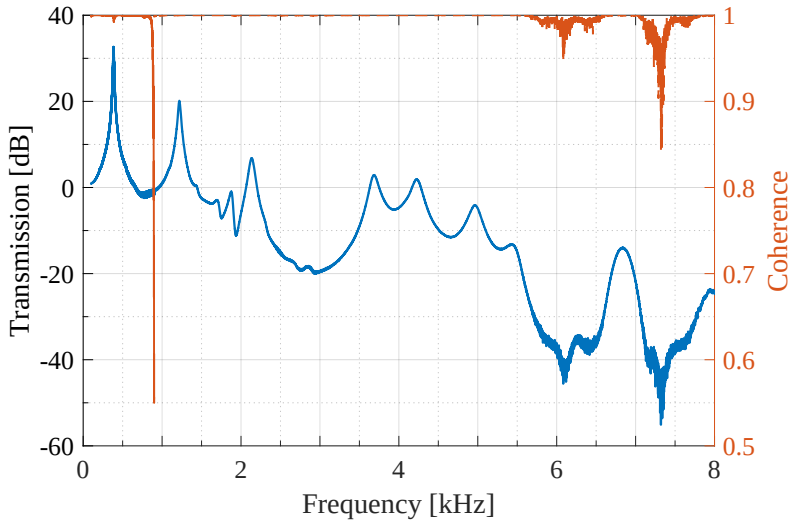

Figure 8: Measured transmission (blue) and coherence spectrum (red) for the SLA-printed lattice arrangement stemming from three KELVIN cell units twisted by $45°$ as shown in Fig. 7. The coherence was computed respectively from the in- and output velocity measurements at the bottom and top plate.

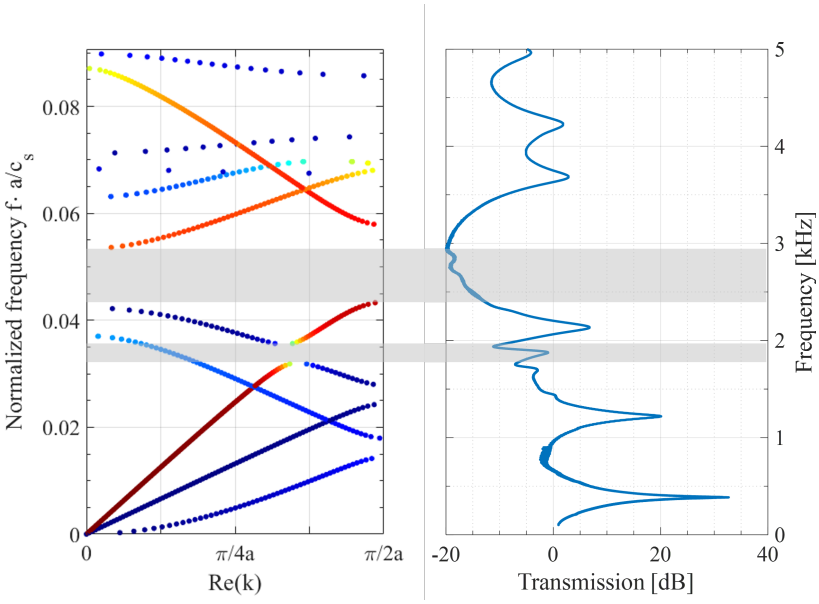

Figure 9: Comparison of the band layout presuming infinite periodicity and the measured transmission spectrum obtained from three periodically arranged unit cells shown in Fig. 7. The color-coding in the band structure highlights the mode polarization.

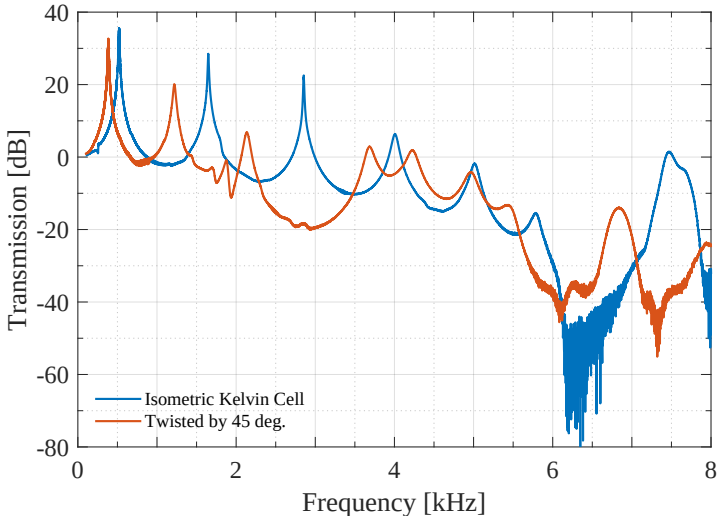

Figure 10: Measured transmission spectra of lattice arrangements stemming from the isometric KELVIN cell and the $45°$-twisted arrangement as shown in Fig. 7. Both structures have the same size but vary in their underlying spatial periodicity pattern.

to its pendant structure resulting from the isometric KELVIN cell . Both structures have the same length; however, the twisted arrangement consists of three periodic repetitions owing to the super cell approach, while six KELVIN cell units form the other array. The comparison of both spectra suggests that the twisting approach can effectively improve the vibro-aoustic response at targeted frequencies in terms of reduced wave transmission. Around the frequency of 2.9 kHz, the template structure exhibits its third peak at 20 dB amplification. In contrast, BRAGG scattering is activated in the twisted arrangement at the same frequencies, leading to a reduction of -20 dB.

4.4 Comparison with numerically computed transmission spectra

The band layout and measured transmission spectra in Fig. 9 show good overall conformity in terms of predicted attenuation regions; however, the comparison does not allow quantitative statements to be made about the frequency match. On the one hand, infinite- and finite-periodic structures are compared; on the other hand, the dispersion analysis assumes linear-elastic material behaviour. Therefore, the transmission analysis was conducted numerically and compared to the measurement data to investigate the transmission characteristics of manufactured and 3D-printed lattice structures in quantitative terms. Numerical transmission spectra were obtained by solving a forced vibration problem in the frequency domain using the Finite-Element framework in COMSOL MULTIPHYSICS. The CAD-based geometry files of manufactured lattice structures were imported into the software and discretized with tetrahedral elements. At the bottom plate, a harmonic prescribed displacement condition $u_{\mathrm{in}} = u_{0,z}\exp(\mathrm{i}\omega\mathrm{t})$ in axial z-direction was imposed. All other boundaries are treated as traction-free. A mass contribution was added at the bottom plate to consider the inertia of the screw junction used in the experiments. Axial displacements around the center point of the top plate were extracted such that numerical transmission values are calculated as $20\log_{10}(\overline{u}_{z,\mathrm{out}}/\overline{u}_{\mathrm{in}})$, where the subscript refers to the surface average at the bottom and top plate areas, respectively.

Fig. 11a compares the computed transmission assuming linear-elastic material behaviour with the measured spectrum. While the curves agree to a reasonable degree in the low-frequency regime, the simulation underestimates the first transmission drop at 2 kHz. The mismatch continues to grow with frequency such that the second and third transmission drops resulting from BRAGG-scattering at high frequencies strongly differ from the measurement. As a result, the effective attenuation frequency ranges between the simulation and the manufactured prototype deviate substantially. Two different causes may be attributed to the deviations: First, the simulation does not include the coupling between the vibration exciter and specimen and assumes a perfectly centered excitation. In the experiments, the excitation is imperfect and inevitably impacts the

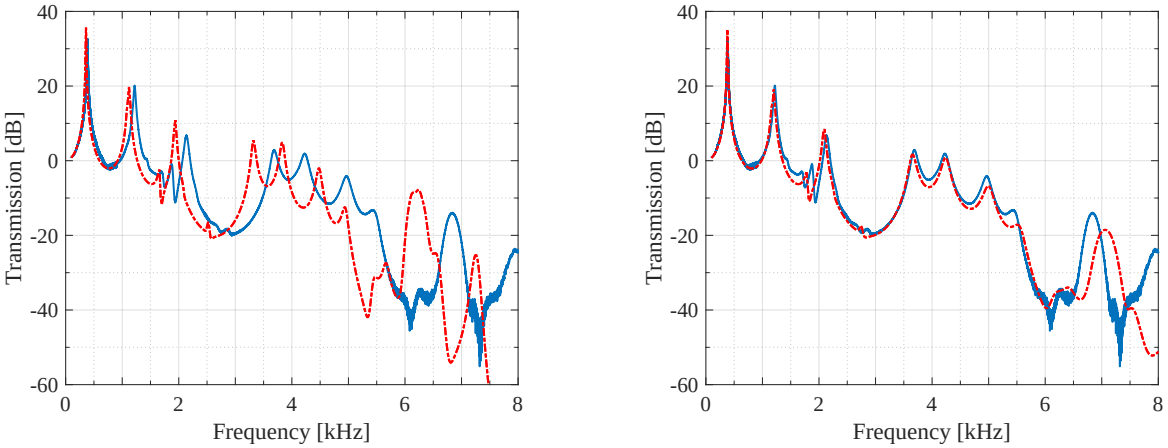

(a) linear-elastic material behavior (b) frequency-dependent YOUNG'S modulus & loss factor

Figure 11: Comparison of the measured transmission spectrum of the finite-size structure presented in Fig. 7 (solid blue) to numerical transmission spectra (red-dashed) employing different behaviours of the same constituent polymer material.

structure along non-axial directions, which may trigger additional modes, e.g. high-frequency ones which are strongly localised in the ligaments. Second, the simulation disregards visco-elastic and frequency-dependent material behaviour of the base polymer, as reported in similar studies [25, 26]. To account for the latter reason, linear frequency-dependent YOUNG'S modulus and structural loss factor were applied in the simulation, as experimentally observed by ARRETCHE *et al.* [26]. Following this reference, the corresponding parameters are set, in a first approximate correction, to $E(f) = E_0 + f \cdot 100\ [\mathrm{kPa/Hz}]$ and $\eta(f) = \eta_0 + f \cdot 10^{-6}\ [1/\mathrm{Hz}]$, with E_0 and η_0 being the nominal values of the linear-elastic case. The frequency factors of both material parameters were calibrated to obtain a close match between experimental and numerical transmission data. The boundary conditions remain unchanged, while the mass is corrected by reducing the material density by 10% compared to the nominal values suggested by the manufacturer. Fig. 11b reports the measured transmission spectrum compared to numerical values assuming frequency-dependent material behaviour. The resulting curves show a very good agreement in the considered frequency range; in particular, the simulation closely captures the first and second transmission dips around 2 kHz and 5.5 kHz. The simulation overestimates the opening of the third dip at 7 kHz; here, the linear frequency dependence no longer appears to be an accurate material model and requires further adjustment, e.g. by considering more detailed visco-elastic models. The comparison confirms that the deviations observed in the initial linear-elastic case can be attributed to the material behaviour of the base polymer. Especially in the high-frequency regime, more in-depth material characterisation is required to map the vibration attenuation features of manufactured prototypes.

5 Conclusion

This contribution proposes cellular lattice units stemming from the KELVIN cell as building blocks for periodic microstructures. By introducing so-called *twists* on the square faces of the KELVIN cell , the unit cell geometry and symmetry characteristics can be varied as a function of the chosen twist angle and direction. The proposed approach offers a variety of possibilities for changing the lattice architecture in a controlled manner and observing the resulting mechanical properties –such as band gap behavior for vibration attenuation– as a function of the change at the microstructural level.

The mentioned vibration attenuation functionality is investigated by considering the elastic wave propagation in two selected lattice configurations extended periodically to infinity along one direction. It is demonstrated that modifying the KELVIN cell using the twisting approach generates frequency band gaps stemming from BRAGG scattering and coupling of counter-propagating waves. The induced gaps are absent in the template geometry and are tunable to a limited extent in terms of their width and center frequency by varying the twist

angle. The experimental investigation demonstrated that the proposed lattice structures are manufacturable and of sufficient quality using an ordinary stereolithographic 3D printer. Transmission measurements on finite-periodic samples confirmed the vibration attenuation capacities of twisted geometries, with attainable attenuation of up to -20 dB for arrays consisting of three unit cells.

However, the numerical transmission analysis revealed that assuming linear-elastic material behavior of the constituent polymer material underestimates the frequency regions exhibiting significant vibration attenuation in the measurements. This misprediction requires accounting for the frequency-dependency of the polymer base material. In this study, a close prediction of the measured and simulation transmission characteristics was achieved by considering a linear frequency dependency of the elasticity modulus and structural loss factor.

Acknowledgements

The manufacturing and measurements were conducted at the Department for Computational Mechanical and Materials Engineering at the University of Groningen. The authors would like to thank Anastasiia Krushynska and Shantanu Nath from the METAMECHANICS group for the possibility of using the laboratory facilities and for their continuous support and supervision of the campaign. The authors would also like to gratefully acknowledge the financial support provided by the Swedish Research Council (VR Grant 2021-05791).

References

[1] M. Eder, S. Amini, and P. Fratzl, "Biological composites-complex structures for functional diversity," *Science (New York, N.Y.)*, vol. 362, no. 6414, pp. 543–547, 2018.

[2] R. Craster, S. Guenneau, M. Kadic, and M. Wegener, "Mechanical metamaterials," *Reports on progress in physics. Physical Society (Great Britain)*, vol. 86, no. 9, 2023.

[3] T. A. Schaedler and W. B. Carter, "Architected cellular materials," *Annual Review of Materials Research*, vol. 46, no. 1, pp. 187–210, 2016.

[4] T. Bückmann, M. Thiel, M. Kadic, R. Schittny, and M. Wegener, "An elasto-mechanical unfeelability cloak made of pentamode metamaterials," *Nature communications*, vol. 5, 2014.

[5] Z. Wang, C. Luan, G. Liao, J. Liu, X. Yao, and J. Fu, "Progress in auxetic mechanical metamaterials: Structures, characteristics, manufacturing methods, and applications," *Advanced Engineering Materials*, vol. 22, no. 10, 2020.

[6] C. C. Claeys, K. Vergote, P. Sas, and W. Desmet, "On the potential of tuned resonators to obtain low-frequency vibrational stop bands in periodic panels," *Journal of Sound and Vibration*, vol. 332, no. 6, pp. 1418–1436, 2013.

[7] C. Claeys, E. Deckers, B. Pluymers, and W. Desmet, "A lightweight vibro-acoustic metamaterial demonstrator: Numerical and experimental investigation," *Mechanical Systems and Signal Processing*, vol. 70-71, no. 8, pp. 853–880, 2016.

[8] S. Krödel, T. Delpero, A. Bergamini, P. Ermanni, and D. M. Kochmann, "3d auxetic microlattices with independently controllable acoustic band gaps and quasi-static elastic moduli," *Advanced Engineering Materials*, vol. 16, no. 4, pp. 357–363, 2014.

[9] L. Junyi and D. S. Balint, "A parametric study of the mechanical and dispersion properties of cubic lattice structures," *International Journal of Solids and Structures*, vol. 91, no. 1838, pp. 55–71, 2016.

[10] M. Mazzotti, A. Foehr, O. R. Bilal, A. Bergamini, F. Bosia, C. Daraio, N. M. Pugno, and M. Miniaci, "Bio-inspired non self-similar hierarchical elastic metamaterials," *International Journal of Mechanical Sciences*, vol. 241, 2023.

[11] A. H. Orta and C. Yilmaz, "Inertial amplification induced phononic band gaps generated by a compliant axial to rotary motion conversion mechanism," *Journal of Sound and Vibration*, vol. 439, pp. 329–343, 2019.

[12] C. Yilmaz, G. M. Hulbert, and N. Kikuchi, "Phononic band gaps induced by inertial amplification in periodic media," *Physical Review B*, vol. 76, no. 5, 2007.

[13] A. Bergamini, M. Miniaci, T. Delpero, D. Tallarico, B. van Damme, G. Hannema, I. Leibacher, and A. Zemp, "Tacticity in chiral phononic crystals," *Nature communications*, vol. 10, no. 1, 2019.

[14] I. Fernandez-Corbaton, C. Rockstuhl, P. Ziemke, P. Gumbsch, A. Albiez, R. Schwaiger, T. Frenzel, M. Kadic, and M. Wegener, "New twists of 3d chiral metamaterials," *Advanced materials (Deerfield Beach, Fla.)*, vol. 31, no. 26, 2019.

[15] H. Mao, R. Rumpler, M. Gaborit, P. Göransson, J. Kennedy, D. O'Connor, D. Trimble, and H. Rice, "Twist, tilt and stretch: From isometric kelvin cells to anisotropic cellular materials," *Materials & Design*, vol. 193, p. 108855, 2020.

[16] H. Mao, R. Rumpler, and P. Göransson, "An inverse method for characterisation of the static elastic hooke's tensors of solid frame of anisotropic open-cell materials," *International Journal of Engineering Science*, vol. 147, no. 1–2, 2020.

[17] M. I. Hussein, "Reduced bloch mode expansion for periodic media band structure calculations," *Proceedings of the Royal Society A: Mathematical, Physical and Engineering Sciences*, vol. 465, no. 2109, pp. 2825–2848, 2009.

[18] B. Yuan, V. F. Humphrey, J. Wen, and X. Wen, "On the coupling of resonance and bragg scattering effects in three-dimensional locally resonant sonic materials," *Ultrasonics*, vol. 53, no. 7, pp. 1332–1343, 2013.

[19] A. O. Krushynska, A. S. Gliozzi, A. Fina, D. Krushinsky, D. Battegazzore, M. A. Badillo-Ávila, M. Acuautla, S. Stassi, C. Noè, N. M. Pugno, and F. Bosia, "Dissipative dynamics of polymer phononic materials," *Advanced Functional Materials*, vol. 31, no. 30, 2021.

[20] L. Iorio, J. M. de Ponti, A. Corigliano, and R. Ardito, "Bandgap widening and resonator mass reduction through wave locking," *Mechanics Research Communications*, vol. 134, 2023.

[21] O. Giannini and A. Sestieri, "Experimental characterization of veering crossing and lock-in in simple mechanical systems," *Mechanical Systems and Signal Processing*, vol. 72-73, pp. 846–864, 2016.

[22] N. C. Perkins and C. D. Mote, "Comments on curve veering in eigenvalue problems," *Journal of Sound and Vibration*, vol. 106, no. 3, pp. 451–463, 1986.

[23] Y. Achaoui, A. Khelif, S. Benchabane, and V. Laude, "Polarization state and level repulsion in two-dimensional phononic crystals and waveguides in the presence of material anisotropy," *Journal of Physics D: Applied Physics*, vol. 43, no. 18, 2010.

[24] B. R. Mace and E. Manconi, "Wave motion and dispersion phenomena: veering, locking and strong coupling effects," *The Journal of the Acoustical Society of America*, vol. 131, no. 2, pp. 1015–1028, 2012.

[25] A. O. Krushynska, N. Anerao, M. A. Badillo-Ávila, M. Stokroos, and M. Acuautla, "Arbitrary-curved waveguiding and broadband attenuation in additively manufactured lattice phononic media," *Materials & Design*, vol. 205, 2021.

[26] I. Arretche and K. H. Matlack, "Experimental testing of vibration mitigation in 3d-printed architected metastructures," *Journal of Applied Mechanics*, vol. 86, no. 11, 2019.